V European Conference on Computational Fluid Dynamics
ECCOMAS CFD 2010
J. C. F. Pereira and A. Sequeira (Eds)
Lisbon, Portugal,14-17 June 2010

AN NUMERICAL INVESTIGATION OF THE TURBULENT FLOWS USING THE DETACHED-EDDY SIMULATION

K. Fraňa and V. Honzejk

Department of Power Engineering Equipment, Technical University of Liberec,
Studentska 2, Liberec, 461 17, Czech Republic
e-mail: karel.frana@seznam.cz, vit.honzejk@seznam.cz

Key words: Detached Eddy Simulations, Finite-Element Method, Flow past a cylinder, Code validations

Abstract. *The turbulent flow is investigated numerically using the in-house computational code based on the Finite-Element Method with pressure-stabilized Petrov-Galerkin and Streamline Upwind Petrov-Galerkin schemes. The flow problem is represented by a three-dimensional unsteady turbulent flow past a circular cylinder at Reynolds number 3.900 and 140.000, respectively. The turbulent flow behavior is captured numerically using the hybrid URANS/LES turbulent model group, particularly, represented by the Delayed-Detached-Eddy Simulation (DDES) approach. The performed grid study reveals significant feature of the grid resolution effect in the spanwise dimension on the time-averaged flow behavior and statistical flow results. Finally, obtained numerical results calculated by DDES are generally in good agreement with experimental data and other numerical results in respect to the time-averaged velocity field, Strouhal number, drag coefficient and partially Reynolds shear stress distribution even for relatively coarse computational grid used for numerical calculation.*

1 INTRODUCTION

Turbulent flows is characterized by complex three-dimensional flow phenomena consisting effects such as flow separations, quasi-periodic vortex shedding, multiple recirculation zones, wake structures etc.. Recently, various numerical turbulent methods have been more or less successfully applied for turbulent flow calculations, particularly based on the steady or unsteady Reynolds-averaged Navier-Stokes (RANS or URANS) approach, Large Eddy Simulation (LES), blended RANS-LES models or even Direct Numerical Simulation (DNS). The significant progress has been reached especially in hybrid RANS-LES models commonly applied for higher Reynolds number massively separated flows. The most popular approach of this group is Detached-Eddy Simulation (DES) originally proposed by Spalart et. al.[5] hereafter referred to as DES97 or easily DES. An advantage of DES is the easy of programming and applications for a complex-geometry. The brief summary about DES applications in various flow problems can be found in publication[17].
A general feature of this particular approach is that the whole a major part of the attached boundary layer is treated by RANS or URANS as a quasi-steady, while LES concept is applied only in the separated flow regions. By consensus, the sooner this takes place, then better. Unfortunately, standard DES formulation on typical grids does not achieve this switch very fast all[3,17]. The space between two areas treated by LES or RANS is known as the grey area and therefore the grey area effects is mostly used for a switch procedure between LES and RANS calculation and it will be discussed later in details. In practice, DES approach is based on the one-equation Spalart-Allmaras eddy viscosity model and it has been successfully applied e.g. to resolve rich dynamics of coherent structures over complex geometrical configurations at practical Reynolds numbers[16]. In spite of the promise of this stable and accurately acceptable approach, however, at least two weakness of this model are well known and already discussed extensively. Firstly, the strong dependence of the DES approach on the grid structure has been recognized even by Spalart and discussed in details later e.g. by Paik[16].The second deficiency of DES is caused by the fact that the subgrid eddy viscosity decreases with both decreasing grid spacing and local flow Reynolds number. Consequently, the fast nonlinear drop of turbulent viscosity gives rise to a premature switch between LES and URANS especially in the region of the flow, where the local Reynolds number is sufficiently low. This problem is called as modeled-stress depletion (MSD) and a consequence of that is called as grid-induced separation (GIS)[17]. This situation illuminated above can typically occur, for instance, in the downstream region of surface-mounted obstacles. The concept study of the switch between LES and URANS approach called as grey area effect in dependence of the grid construction has been presented and discussed in Travin et al.[4] and Spalart et. al.[3] etc.. Because of the fact that the classical DES approach suffers from various deficiencies e.g. early separation etc., the new standard version of DES so called Delayed-Detached-Eddy Simulation has been proposed. In this new concept, the limiter for the switch between LES and RANS depends not only on the grid size but as well on the

solution[17]. Consequently, DDES has demonstrated a potentiality to resolve grid-induced separation, without impending LES function after separation.
The objective of this paper is the implementation of the turbulent model (DDES) into the in-house computation code, the appropriate code testing and application for a complex three- dimensional turbulent flow simulation. The code testing is carried out on the benchmark represented by the turbulent flow over a circular-cylinder. This particular flow problem has been studied numerically e.g. using the Large-Eddy Simulation (LES) by Breuer[1,2] for Reynolds numbers 3.900. The found results were in good agreement with experiments in sense of predictions of the drag and pressure coefficients, mean velocity field distribution, Strouhal number and resolved Reynolds shear stress. The study of the flow with the turbulent-separation region at Reynolds number 140.000 has been documented in Breuer[2]. In the frame of this study, the influence of the subgrid scale modeling and grid resolution on the quality of the predicted results were investigated. In general, the found LES results were in satisfactory agreement with experimental data, however, the big computation effort was simultaneously required to resolve accurately the flow in the near-wall region. As a practical solution, the DES used for higher Reynolds number flow is getting a powerful alternative approach. Travin[4] performed a numerical study using DES for flow around a circular cylinder in a uniform cross-flow and the Reynolds number varied from 50.000 up to 3×10^6. The results were in good agreement with experimental results for drag, shedding frequency, pressure and skin friction, however, disagreement up to 30% to experiment was found in the prediction of the bubble length and in the Reynolds stress distribution. The brief of the existing experimental and numerical results of the flow past a circular cylinder for $Re = 3.900$ and $Re = 140.000$ is summarized in Fureby[14].
The paper is organized as follows: In Section 2, the objective of the flow study including the basic equation system represented by Navier-Stokes equation and by turbulent approach is introduced. Details about numerical method and its application in the in-house computational code are presented in Section 3. Section 4 summarizes important numerical results and the comparison with experimental data and with other previous numerical results. Finally, in Section 5, significant conclusions are reported.

2 PROBLEM FORMULATION

An incompressible turbulent flow with the constant material properties such as molecular kinematic viscosity ν and density ρ is considered. The unsteady flow behavior is governed by Navier-Stokes and continuity equations taking the form

$$\frac{\partial \boldsymbol{u}}{\partial t} + \nabla \cdot \boldsymbol{u}\boldsymbol{u} = -\nabla p + \nabla \left(\nu + \nu_t\right) \nabla \boldsymbol{u} \quad (1)$$

$$\nabla \cdot \boldsymbol{u} = 0 \quad (2)$$

with Dirichlet and Neumann type boundary conditions

$$\boldsymbol{u} = \boldsymbol{g} \quad \text{at} \quad \Gamma_g \tag{3}$$

$$\boldsymbol{n} \cdot [p + (\nu + \nu_t) \nabla \boldsymbol{u}] = \boldsymbol{h} \quad \text{at} \quad \Gamma_h \tag{4}$$

where $\boldsymbol{u}$ is the velocity, t time, p pressure divided by density ρ, and ν_t is a turbulent eddy viscosity, respectively. The effect of turbulence in flows is represented by a turbulent eddy viscosity. Particularly, in the DDES approach the calculation of the turbulent eddy viscosity is based on a modified eddy viscosity calculated by the transport equation defined in the Spalart-Allmaras model[5] as follows

$$\frac{D\widetilde{\nu}}{Dt} = c_{b1}\widetilde{S}\widetilde{\nu} + \frac{1}{\sigma}\left[\nabla \cdot ((\nu + \widetilde{\nu})\nabla\widetilde{\nu}) + c_{b2}(\nabla\widetilde{\nu})^2\right] - c_{w1} f_w \left[\frac{\widetilde{\nu}}{d}\right]^2 \tag{5}$$

where the right-hand side includes the production term, the diffusion term and the destruction term for the reduction of the stresses in the vicinity near the solid walls. The production term includes further the scalar quantity $\widetilde{S}$ which is expressed by a magnitude of vorticity S plus a near-wall correction and it can be modeled as in the original Spalart-Allmaras model[5] leading to the form

$$\widetilde{S} \equiv S + \left(\frac{\widetilde{\nu}}{\kappa^2 d^2}\right) f_{v2} \tag{6}$$

Equation 5 must be closed with the auxiliary relations and constants that can be found e.g. in publication[5]. The desired turbulent eddy viscosity ν_t is calculated by the modified turbulent viscosity using the relation taking the form of

$$\nu_t = \widetilde{\nu} f_{v1} \tag{7}$$

In the DES approach, the wall distance is replaced by a characteristic length scale $\widetilde{d}$ proportional to Δ so that

$$\widetilde{d} \equiv min(d, C_{DES}\Delta), \quad \Delta \equiv max(\Delta x, \Delta y, \Delta z) \tag{8}$$

The recommended value for the adjustable parameter is CDES=0.65[6]. The weakness of the classical DES formulation is an unphysical behavior in the attached boundary layers relating to so called grey zone. To suppress the negative effect, various modifications of the DES formulation were proposed, for instance, the DDES model. Particularly, a new function f_d was additionally used for the definition of the characteristic length scale so that the dissipation length scale is now in the form

$$\widetilde{d} = d - f_d max\left(0; d - C_{DES}\Delta\right) \tag{9}$$

where

$$f_d = 1 - tanh\left[(8r_d)^3\right] \tag{10}$$

and

$$r_d = \frac{\nu + \nu_t}{\sqrt{\partial x_j u_i \partial x_j u_j}\kappa^2 d^2} = \frac{\widetilde{\nu}}{S\kappa^2 d^2} \tag{11}$$

From the practical point of view, the main objective of this modification is to prevent earlier switch from URANS approach to LES model occurring in the attached boundary layer as it has been reported in the previous section.

3 NUMERICAL METHODS

The finite element discretization space of Ω with the boundary Γ is consisted of Ω_e , where $e = 1, 2, n_{el}$ and n_{el} is the number of elements. The weighting function in Eq. 12 is expressed as $\boldsymbol{w}^h$ and q^h, respectively. Equations 1 and 2 can be formally integrated in time and written in form as follows

$$\int_\Omega \boldsymbol{w}^h \left(\frac{\boldsymbol{u}^{n+1} - \boldsymbol{u}^n}{\Delta t} + \nabla \cdot \bar{\boldsymbol{u}}\bar{\boldsymbol{u}} + \nabla \bar{p} \right) d\Omega + \int_\Omega \left(\nabla \boldsymbol{w}^h \right)^T : (\nu_c)\, \nabla \bar{\boldsymbol{u}} d\Omega -$$
$$\int_\Gamma \boldsymbol{w}^h \cdot (\nu_c)\, \partial_n \boldsymbol{u} d\Gamma + \int_{d\Omega} q^h \nabla \cdot \boldsymbol{u}^{n+1} d\Omega + \sum_{e=1}^{n_{el}} \int_{d\Omega^e} \left(\tau_{SUPG} \bar{\boldsymbol{u}} \cdot \nabla \boldsymbol{w}^h \right) \cdot (\bar{\boldsymbol{r}})\, d\Omega +$$
$$\sum_{e=1}^{n_{el}} \int_{d\Omega^e} \left(\tau_{PSPG} \nabla q^h \right) \cdot (\bar{\boldsymbol{r}})\, d\Omega = 0 \tag{12}$$

where the residual $\bar{\boldsymbol{r}}$ is defined as

$$\bar{\boldsymbol{r}} = \partial_t \bar{\boldsymbol{u}} + \nabla \cdot \bar{\boldsymbol{u}}\bar{\boldsymbol{u}} - \nabla \left[(\nu + \nu_t) \nabla \bar{\boldsymbol{u}} \right] + \nabla \bar{p} \tag{13}$$

The overbar denotes the time averaged over the time interval given by t_n and t_{n+1}. Because of the equal-order interpolation function used for velocity and pressure, the stabilization approach based on the pressure-stabilized Petrov-Galerkin scheme is applied. Moreover, for higher Reynolds number flows, the additional streamline upwind Petrov-Galerkin stabilization approach is adopted. Appropriate choice of the stabilization constant τ_{SUPG} and τ_{PSPG} is given in publication[10]. The momentum equation integrated in Eq. 12 can be split into a velocity (predictor) and a pressure (corrector) step. The velocity predictor term is formulated symbolically as follows

$$\boldsymbol{U}^* = \boldsymbol{U}_n - dt \boldsymbol{M}_L{}^{-1} \left[\boldsymbol{A} \cdot \boldsymbol{U}\boldsymbol{U} + \left(\boldsymbol{L}^{\nu_c} + \boldsymbol{L}_\Gamma{}^{\nu_c} \right) \boldsymbol{U} \right] + \boldsymbol{T}_{SUPG} \tag{14}$$

where $\boldsymbol{U}^*$ is preliminary estimation of the velocity, $\boldsymbol{M}_L{}^{-1}$ is lumped mass matrix, $\boldsymbol{A}$ is a gradient matrix, $\boldsymbol{L}^{\nu_c}$ is a Laplace matrix and related boundary matrix $\boldsymbol{L}_\Gamma{}^{\nu_c}$. The last term T_{SUPG} is an additional term representing the SUPG stabilization. The corrector step consists pressure equation and correction step of the velocity field calculation. The both equations are in the form

$$\left[(1-\delta)\, \boldsymbol{A} \boldsymbol{M}_L{}^{-1} \boldsymbol{A} + \delta \boldsymbol{L} \right] P = -\boldsymbol{A}\boldsymbol{U}^*/dt \tag{15}$$
$$\boldsymbol{U}^{n+1} = \boldsymbol{U}^* - dt \boldsymbol{M}_L{}^{-1} \boldsymbol{A} P \tag{16}$$

In practice, the predictor step in Eq. 14 is solved explicitly using the Jacobi iterative method, the corrector step involving the pressure equation Eq. 15 is solved implicitly by the Conjugated gradient method. The time-dependent term is discretized by means of the Adam-Bashforth schema. The calculated values e.g. velocity, pressure or turbulent kinetic viscosity are saved at the end of each time step and used as an initial value in the following time step. Taking into account the Neumann boundary type condition (open boundary type condition), the equations of the corrector step are modified and the complete calculation scheme is defined as follows

$$\boldsymbol{U}^{*} = \boldsymbol{U}_{n} - dt{\boldsymbol{M}_{L}}^{-1}\left[\boldsymbol{A}\cdot\boldsymbol{U}\boldsymbol{U} + \left(\boldsymbol{L}^{\nu_c} + \boldsymbol{L}_{\Gamma}{}^{\nu_c}\right)\boldsymbol{U}\right] + \boldsymbol{T}_{SUPG} \tag{17}$$

$$\left[\left(\boldsymbol{A}^{T} - \boldsymbol{G}^{N}\right){\boldsymbol{M}_{L}}^{-1}\left(\boldsymbol{A}^{T} - \boldsymbol{G}^{N}\right) + \delta\boldsymbol{A}{\boldsymbol{M}_{L}}^{-1}\left(\boldsymbol{A}^{T} - \boldsymbol{G}^{N}\right) - \delta\boldsymbol{L}\right]P = \left[\left(\boldsymbol{A}^{T} - \boldsymbol{G}^{N}\right)\boldsymbol{U}^{*} + \boldsymbol{G}^{D}\boldsymbol{U}^{n+1}\right]/dt \tag{18}$$

$$\boldsymbol{U}^{n+1} = \boldsymbol{U}^{*} - dt{\boldsymbol{M}_{L}}^{-1}\left(\boldsymbol{A}^{T} - \boldsymbol{G}^{N}\right)P \tag{19}$$

where G^N is a boundary integral of the Neumann boundary condition and G^D is a boundary integral of the Dirichlet boundary condition, respectively. Figure 1 shows stable results of the streamwise velocity field at the outflow boundary. Because of the numerically stable

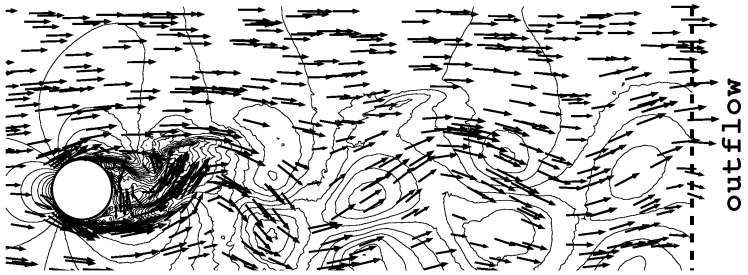

Figure 1: Snapshot of the velocity vector field and velocity lines at the outflow type boundary

form of the Eq. 5, the turbulent model represented by transport equation 5 with auxiliary relations summarized in 6 - 11 is implemented into code without any stabilization approach. This transport equation is solved explicitly using Jacobi method and approximately 9 iterative steps are required to achieve negligible residuals in comparison to the flow solver accuracy. The whole numerical model was implemented on top of the MG grid library[7], which provides data structures, the handling of the unstructured grids and methods for grid adaptations. The parallelization was based on a grid partitioning providing the decomposition of the computational grid into a specific number of partitions. The test of the parallel efficiency was carried out on the cylindrical cavity flow driven by a rotating magnetic field and results were discussed in publication[8]. The code was validated on several tests including a transient channel flow or a flow driven by the rotating magnetic field[18] in the laminar Stokes flow regime. The convergence study proved the

second order accuracy in time and space[8]. In the transient flow regime, the code was validated using the linear stability analysis carried out in the flow driven by the traveling magnetic field[9] and satisfactory results were found in comparison to results provided by calculations based on the high accuracy numerical methods e.g. spectral methods with higher order discretization schemes.

4 RESULTS AND DISCUSSION

The complex three-dimensional flow simulation is carried out at Reynolds number 3.900 (denoted as case LRE) and 140.000 (case HRE) and results are compared with available experimental and numerical results. The computational grids are consisted of the tetrahedral elements with the same grid resolution for all considered test cases. By reason of grid effect study a number of elements in the spanwise dimension of the flow domain varies from 4 up to 32 elements (L/HRE-4, L/HRE-8, L/HRE-16 and L/HRE-32).

4.1 The three-dimensional flow effects

Table 1 reports important physical quantities such as the drag coefficient c_D based on the freestream velocity U_{inlet} nd D, Strouhal number St, bubble length L_R/D (the length of the recirculation bubble, from the base to the zero-mean-velocity point on the centerline) and r.m.s. value of the lift coefficient c_l' calculated on the different spanwise grid resolutions.

The examination of the spanwise grid resolution on the physical quantity points out that the elongation of the computational domain has caused reduction of the pressure coefficient value, Strouhal number and r.m.s. value of the lift coefficient and this observation is fully consistent with Breuer[1,2]. Note, in accordance with Breuer[1] study, the size elongation of the computational domain in the streamwise and crossflow dimension may evoke the similar effect as that described above. The found drag coefficient $c_D = 1.02$ at

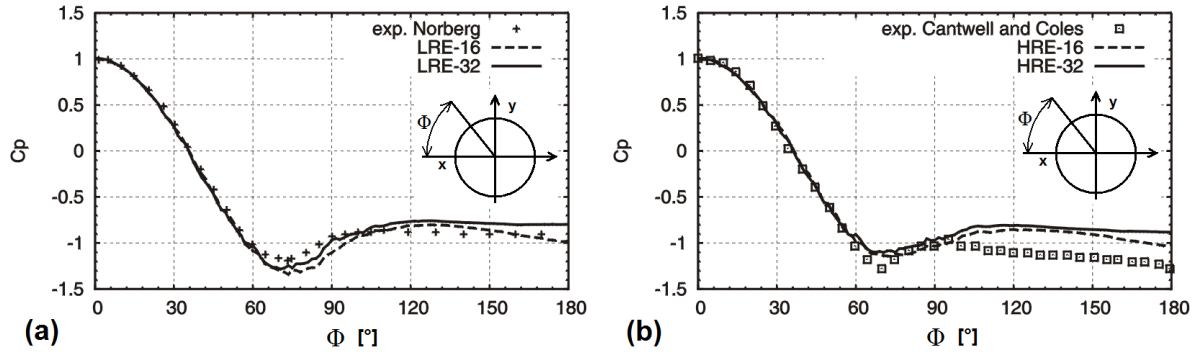

Figure 2: Pressure coefficient c_p in comparison with experimental data[12,13] for (a) Re=3.900, (b) Re=140.000

Reynolds number 3.900 corresponds well to values from Breuer[1] ($c_D = 1.01 - 1.1$) and it is

Case	points	c_D	L_R/D	St	c_l'
LRE-4	67133	1.57	0.88	0.23	1.17
LRE-8	125641	1.37	1.00	0.23	0.86
LRE-16	232707	1.25	1.05	0.22	0.73
LRE-32	448304	1.02	1.53	0.21	0.37
Breuer[1]-LES	165x165x32	1.01/1.1	0.99/1.4	-	-
Breuer[1]-LES	165x165x1	1.625	-	-	-
Son et al.[1]	experiment	0.97/0.99	1.1/1.53	-	-
Dong[12]-DNS	902(8)x(64-192)	-	1.0/1.18	0.203/0.21	-
HRE-4	67133	1.52	1.02	0.25	1.01
HRE-8	125641	1.4	1.09	0.24	0.77
HRE-16	232707	1.38	1.09	0.24	0.68
HRE-32	448304	1.24	1.4	0.22	0.40
Breuer[2]-LES	325x325x64	1.22/1.45	0.3/0.38	0.20/0.22	-
Travin[4]-DES	118x109x30	0.87/1.08	1.1/1.5	0.21/0.23	0.1/0.3
Cantwell et al.[13]	experiment	1.237	0.44	0.18	-

Table 1: Summarization of the physical quantities for DES,LES and DDES studies, experiments and for Reynolds numbers 3.900 (LRE) and 140.000 (HRE).

also relatively in good agreement to experiment[1]. At the same Reynolds number level, the Strouhal number is found to be St=0.21 which is in good agreement to the DNS results[12] (St=0.203-0.21). At Re=140.000, the identified Strouhal number is about St=0.22 and that it is in a good agreement with the numerical study in Breuer[2] (St=0.2-0.22) and Travin[4] (St=0.21-0.23). The drag coefficient at the same Re is detected as $c_D = 1.24$ and it is in excellent match to experiment[13] ($c_D = 1.237$) and numerical calculation by Breuer[2] ($c_D = 1.22 - 1.45$). For LRE case, the bubble length is about 1.53, however, for coarse spanwise grid resolution it is about 1.05 and less. Therefore, the computation preformed on the coarse spanwise grid resolution provides better results then finer grid. For HRE case, the found bubble lengths for all here considered spanwise grid resolution are out of the experimental results and numerical simulation[1], but fully consistent to Travin[4] (DES). Figures 2 (a) and (b) indicate the distribution of the pressure coefficient c_p on the surface of the circular cylinder. The flow remains to be laminar in this region and it is solved using URANS approach. The grid refinement in the spanwise dimension has slight influence on the pressure coefficient distribution only in the reattachment region on the circular cylinder. The results obtained show good agreement with experimental results[13], however, at the case HRE a slight deviation from the experimental data is clearly identified in the recirculation region behind a circular cylinder and it was observed in study[4] as well. The current numerical study reveals further, that the effect of the spanwise dimension can be well examined on the resolved Reynolds shear stress in the region near

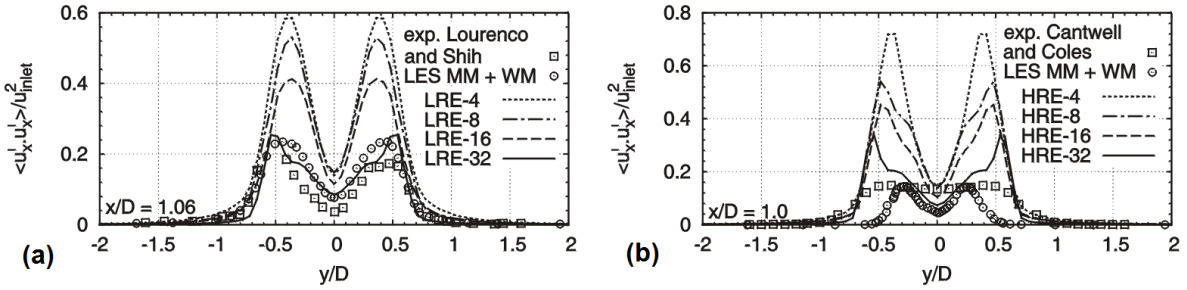

Figure 3: The resolved Reynolds shear stress $< u'_x u'_x >$ compared with experimental[11,13] and numerical[14] data: (a) at x/D=1.06 for Re=3.900 and (b) x/D=1 for Re=140.000

wake of the circular cylinder. At this particular place, the Reynolds shear stress distribution is extremely sensitive on the three-dimensional flow effects even for a wide range of the Reynolds numbers. Figures 3 (a) and (b) show the $< u'_x u'_x >$ component of the resolved Reynolds shear stress at the place $x/D = 1.06$ and at Re=3.900 and $x/D = 1$ at Re=140.000, respectively. Evidently, with increase of the spanwise grid resolution the order of the Reynolds shear stress is decreasing up to reaching a satisfactory results in respect to the experimental[11,13] and other numerical results[14]. However, at the higher Reynolds number, further grid refinement in near wake region is maybe needed, but in accordance to the study by Travin[4], in this study the used higher grid resolution revealed still inconsistence between numerically resolved and experimentally determined Reynolds shear stresses.

4.2 Time-averaged velocity field

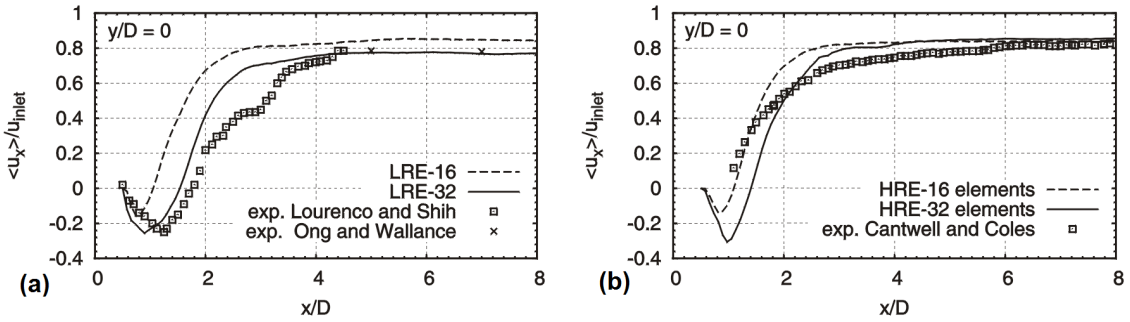

Figure 4: Time-averaged streamwise velocity along the symmetry line compared with experimental results[11,13] for (a) Re=3.900 and (b) Re=140.000

Figure 4 (a) shows the time-averaged streamwise velocity along the symmetry line for Reynolds number 3.900, whereas the results for Reynolds number 140.000 are illustrated in Fig. 4 (b). Calculations performed on the computational grid with 32 elements in the spanwise dimension provides results with the satisfactory agreement with experimental

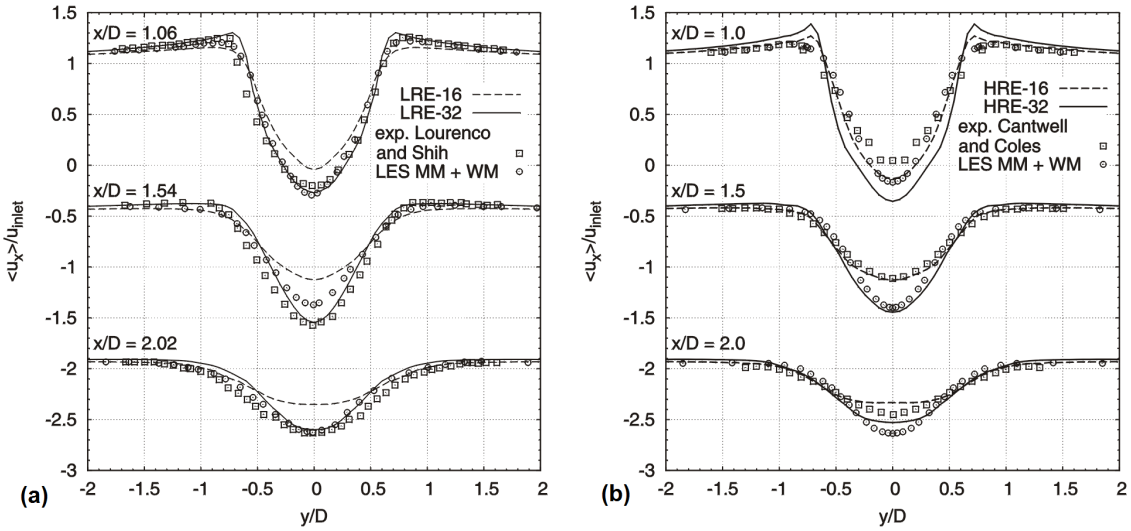

Figure 5: Time averaged streamwise velocity along a constant x-position compared with experimental results[11,13] and numerics[14] for (a) Re=3.900, (b) Re=140.000

data[11,13]. In general, the grid refinement in the spanwise dimension causes an elongation of the recirculation area in the near wake region. Figures 5 (a) and (b) depict the time-average streamwise velocity along a constant x-position. The results calculated on the finer spanwise grid resolution at Reynolds number 3.900 and 140.000 are in good agreement with the experimental data[11,13]. Despite slight overestimation of the velocity in near wake region at Re=140.000, generally, the less time-consuming DDES model provides accurate flow prediction in contrast to the LES approach from the point of the view of the less computational effort and less demand on the grid resolution. The time-averaged normal velocity profiles at constant x-position in the flow wake for Reynolds number 3.900 and 140.000 are plotted in Figure 6 (a) and (b), respectively. The similar results are found in respect to the experimental results[11,13], and especially, in the near wake better results are achieved by DDES calculation in comparison to LES results[15].

4.3 Resolved Reynolds shear stress

Figure 7 (a) and (b) illustrate the resolved streamwise Reynolds shear stress plotted along a constant x-position for Reynolds numbers 3.900 and 140.000, respectively. For low Reynolds numbers (LRE), results are in satisfactory agreement with experimental results[11]. However, for HRE case, the resolved Reynolds shear stresses are completely overestimated in the whole wake region. Albeit the finer grid resolution in the spanwise dimension leaded to the results improvement in the near wake, however, the same grid effect is not detected in the far wake region at all.

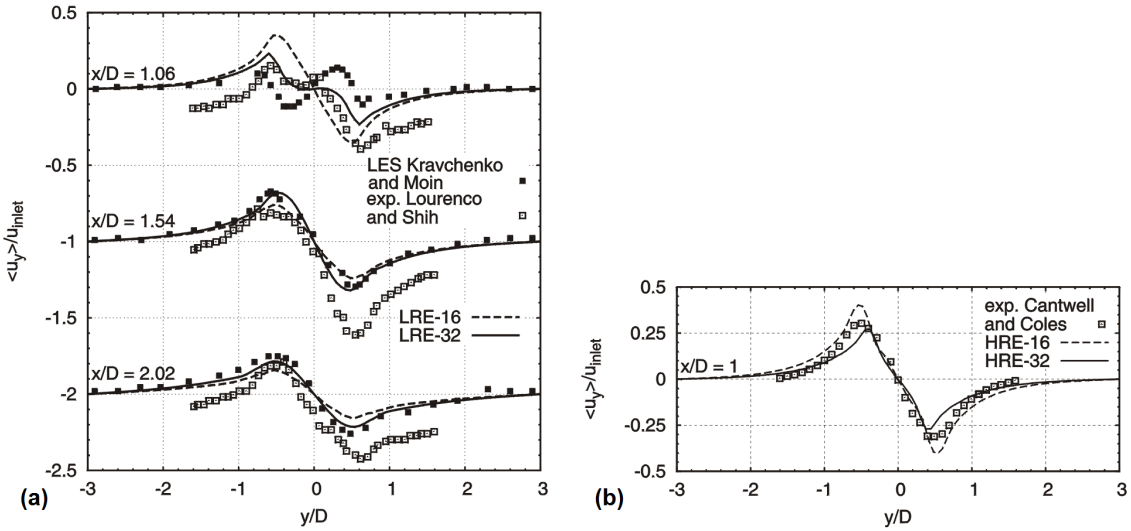

Figure 6: Time-averaged normal velocity along a constant x-position compared with experimental results[11,13] and numerics[15] for (a) Re=3.900 and (b) Re=140.000

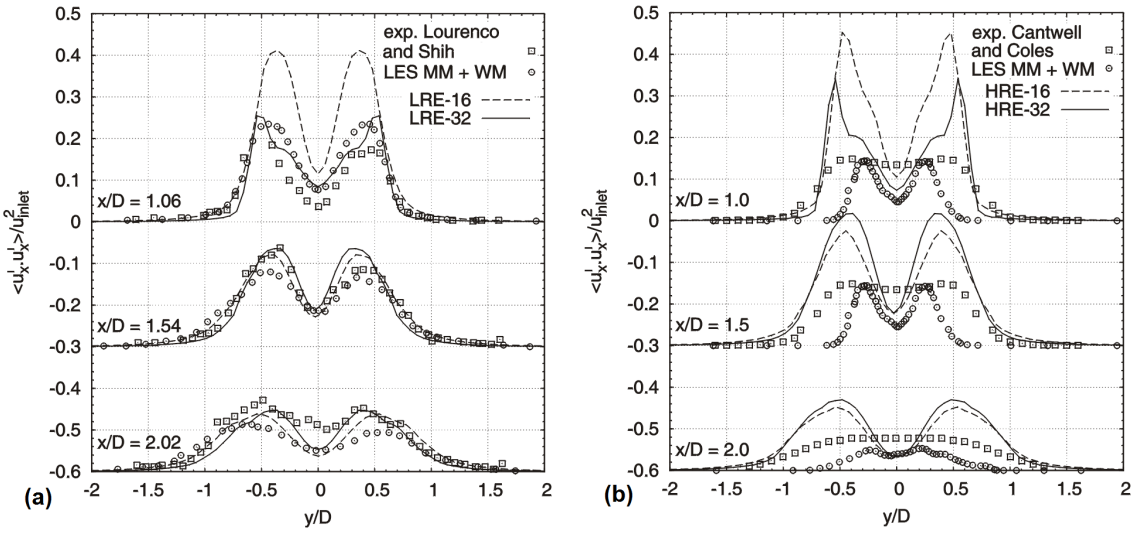

Figure 7: The total resolved Reynolds stress $< u'_x\ u'_x >$ along a constant x-position compared with experimental results[11,13] and numerics[14] for (a) Re=3.900 and (b) Re=140.000

4.4 Frequency and wavenumber spectra

Figures 8 (a) and (b) show wavenumber spectra of the streamwise velocity along the spanwise dimension at the point $x/D = 0.16632$ and $y/D = 0.48$ in the region of the shear layer. For LRE, the power spectra behavior with $p = \frac{5}{3}$ appears at higher wavenumbers (in the inertial subrange or dissipation range), whereas at lower wavenumbers, the spectrum decays slowly and the power law of this decay is affected strongly by the size of the

spanwise dimension of the computational domain. In contrast, in case of the HRE, the energy spectrum exhibits power law behavior with $p = \frac{5}{3}$ in the wide range of wavenumbers, particularly, covering parts of the dissipation and energy-containing range and complete inertial subrange. Furthermore, the elongation of the spanwise dimension does not cause a change of the power law behavior of the energy decay. Figures 9 (a) and (b) illustrate

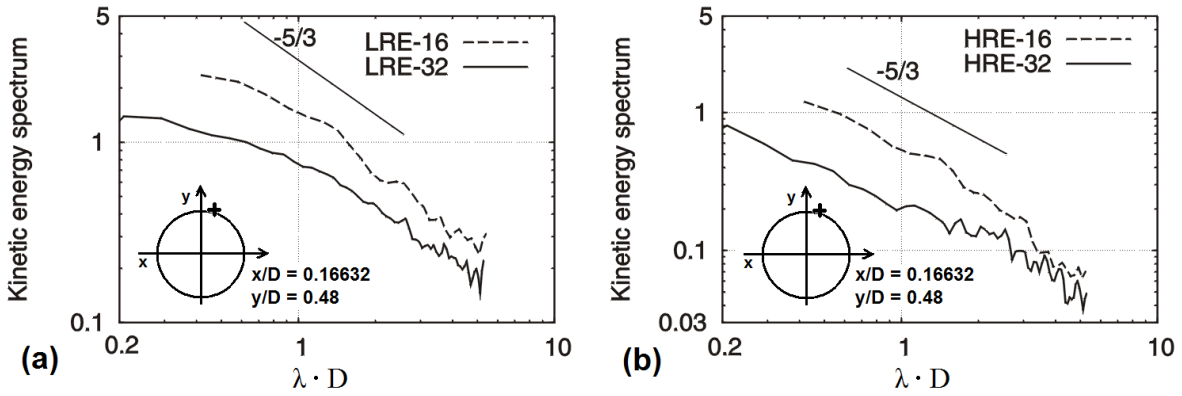

Figure 8: Wavenumber spectra at the position in the shear layer region for Reynolds number (a) 3.900 and (b) 140.000

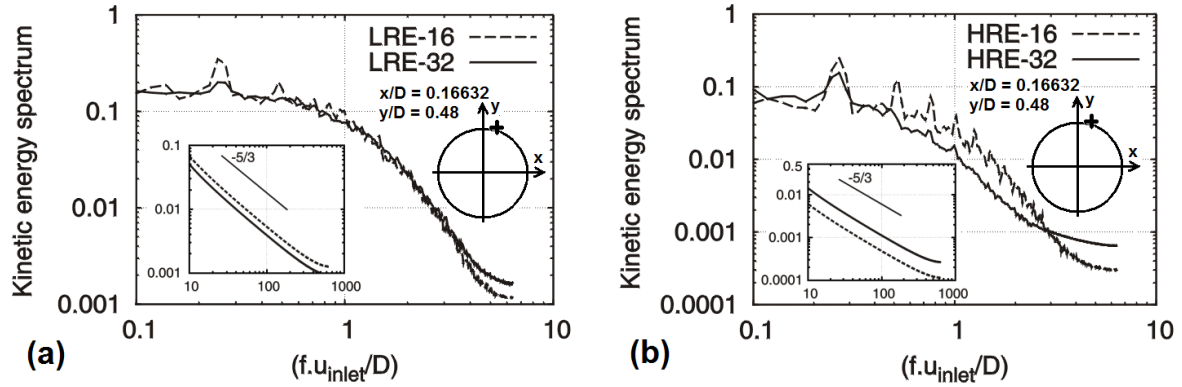

Figure 9: Power energy spectra at the position in the shear layer region for Reynolds number (a) 3.900 and (b) 140.000

power energy spectra of the streamwise velocity at the particular point $x/D = 0.16632$ and $y/D = 0.48$ in the region of the shear layer. The Strouhal frequency has a sharp spectra peak recognizable for both LRE and HRE cases. Because of the spatial locality of the shear-layer vortex[12], no shear-layer vortex frequency appears in the spectra. The power law behavior with $p = \frac{5}{3}$ is detected only in the dissipation range of the wavenumbers for both considered cases LRE and HRE, respectively.

5 CONCLUSION

The presented work is concerning to the isothermal incompressible turbulent flow investigation calculated using the in-house computational code based on the Finite-Element Methods with implemented Delayed-Detached-Eddy Simulation approach and extended recently by open type boundaries. The flow problem represents a turbulent flow past a circular cylinder at lower and higher Reynolds number. The numerically obtained results such as time-averaged velocity field, drag coefficients, Strouhal numbers are mostly in good agreement with experimental data. Despite of the particular overprediction at higher Reynolds number, the used Delayed-Detached Eddy Simulation approach reaches mostly satisfactory results with less computational effort. In contrast to LES approach, the found success results comparison supports the idea to apply this turbulent approach for turbulent flow investigation of the more complex geometry associated with coarse grid resolution. From perspectives, after this successful code validation on the turbulent flow, this model will be used for examination of the turbulent flow driven by a rotating magnetic field in the non-axisymmetrical containers.

ACKNOWLEDGEMENT

Financial support from the particular research grant SGS 2823 at the TU Liberec and from the European Grant CZ.1.07/2.2.00/07.0234 financially supported by the European Union and Ministry of Education of the Czech Republic are gratefully acknowledged.

REFERENCES

[1] M. Breuer, A chalanging test case for large eddy simulation: high Reynolds number circular cylinder flow, *Int. J. of Heat and Fluid Flow*, **21**, 648–654 (2000).

[2] M. Breuer, Large eddy simulation of the subcritical flow past a circular cylinder: Numerical and modeling aspects, *Int. J. for Numer. Meth. Fluids*, **28**, 1281–1302 (1998).

[3] P.R. Spalart, S. Deck, M.L. Shur, K.D. Squires, M. Kh. Strelets and A. Travin, A new version of detached-eddy simulation, resistant to ambiguous grid densities, *Theor. Comput. Fluid Dyn.*, **20**, 181–195 (2006).

[4] A. Travin, M. Shur, M. Strelets and Ph. Spalart, Detached-Eddy Simulations Past a circular cylinder, *Flow, Turbulence and Combustion*, **63**, 293–313 (1999).

[5] P.R. Spalart, S.R. Allmaras, A one-equation turbulence model for aerodynamic flows, *La Recherche Aerospatiale*, 5–21 (1994).

[6] N.V. Nikitin, F. Nicoud, B. Wasistho, K.D. Squires, P.R. Spalart, An approach to wall modeling in large-eddy simulations, *Phys. Fluids*, **12** (2000).

[7] J. Stiller, W.E. Nagel, MG - A Toolbox for Parallel Grid Adaptation and Implementing Unstructured Multigrid Solvers, *In: E.H. D'Hollander et al. (Eds.): Parallel Computing. Fundamentals and Applications*, Imperial College Press (2000).

[8] J. Stiller, K. Fraňa, R. Grundmann, U. Fladrich, W.E. Nagel, A parallel PSPG Finite Element Method for direct Simulation of Incompressible flow, *Euro-Par 2004, Parallel Processing (LNCS 3149)*, edited by M.Danutello, D.Laforenza and M. Vanneschi, Springer-Verlag, 726–733 (2004).

[9] J.Stiller, K. Fraňa, A. Cramer, Transitional and weakly turbulent flow in a rotating magnetic field, *Physics of Fluids*, **19**, 074105 (2006).

[10] T. Tezduyar, Y. Osawa, Finite element stabilization parameters computed from element matrices and vectors, *Comput. Meth. Appl. Mech. Eng.*,**190**, 411–430 (2001).

[11] Lourenco L.M. Shih C., Characteristics of the plane turbulent near wake of a circular cylinder, a particle image velocimetry study, (1993) (data taken from Reference [2]).

[12] Dong S., Karniadakis G.E., Ekmekci A., Rockwell D., A combined direct numerical simulation-particle image velocimetry study of the turbulent near wake, *J. Fluid Mech.*,**569**, 185–207 (2006).

[13] B. Cantwell, D. Coles D., An experimental study on entrainment and transport in the turbulent near wake of a circular cylinder, *J. Fluid Mech.*,**136**, 321–374 (1983).

[14] Ch. Fureby, M. Liefvendahl, U. Svennberg, L. Persson, T. Persson, Incompressible Wall-Bounded Flows, Implicit Large Eddy Simulation: computing turbulent fluid dynamics edited by Fernando F. Grinstein F. F., Len G. Margolin and William J. Rider, *Cambridge University press* (2006).

[15] A.G. Kravchenko, P. Moin, R.D. Moser, Turbulence statistics in fully developed turbulent channel flow at low Reynolds number, *Physics of Fluids*,**12**, 403–417 (2000).

[16] J. Paik, F. Sotiropoulos, F. Port-Agel, Detached eddy simulation of flow around two wall-mounted cubes in tandem, *Int. Journal of Heat and Fluid Flow*, **30**, 286–305 (2009).

[17] Ph.R. Spalart, Detached-Eddy simulation, *Annuv. Rev. Fluid. Mech.*, **41**, 181–202 (2009).

[18] K. Fraňa, J. Stiller, A numerical study of flows driven by a rotating magnetic field in a square container, *European Journal of Mechanics / Fluids B*,**27** 491–500 (2008).